Evidence that filament fracture occurs in an ITER toroidal field conductor after cyclic Lorentz force loading in SULTAN

2012 Supercond. Sci. Technol. 25 075007

(http://iopscience.iop.org/0953-2048/25/7/075007)

Supercond. Sci. Technol. **25** (2012) 075007 (11pp) doi:10.1088/0953-2048/25/7/075007

Evidence that filament fracture occurs in an ITER toroidal field conductor after cyclic Lorentz force loading in SULTAN

Carlos Sanabria[1], Peter J Lee[1], William Starch[1], Ian Pong[2], Alexander Vostner[2], Matthew C Jewell[3], Arnaud Devred[2] and David C Larbalestier[1]

[1] Applied Superconductivity Center, National High Magnetic Field Laboratory, Florida State University, Tallahassee, FL 32310, USA
[2] ITER Organization, Route de Vinon-sur-Verdon, 13115 St Paul-lez-Durance, France
[3] The Materials Science Center, University of Wisconsin-Eau Claire, Eau Claire, WI 54702, USA

E-mail: sanabria@asc.magnet.fsu.edu

Received 31 March 2012, in final form 2 May 2012
Published 29 May 2012
Online at stacks.iop.org/SUST/25/075007

Abstract
We analyzed the ITER TFEU5 cable-in-conduit conductor (CICC) after the full SULTAN conductor qualification test in order to explore whether Lorentz force induced strand movement inside the CICC produces any fracture of the brittle Nb_3Sn filaments. Metallographic image analysis was used to quantify the change in void fraction of each sub-cable (petal); strands move in the direction of the Lorentz force, increasing the void space on the low force side of the CICC and producing a densification on the high force side. Adjacent strand counting shows that local increases in void space result in lower local strand–strand support. Extensive metallographic sampling unambiguously confirms that Nb_3Sn filament fracture occurred in the TFEU5 CICC, but the filament fracture was highly localized to strand sections with high local curvature (likely produced during cabling, where strands are pivoted around each other). More than 95% of the straighter strand sections were free of filament cracks, while less than 60% of the bent strand sections were crack free. The high concentration of filament fractures on the tensile side of the strand–strand pivot points indicates that these pivot points are responsible for the vast majority of filament fracture. Much lower crack densities were observed in CICC sections extracted from a lower, gradient-field region of the SULTAN-tested cable. We conclude that localized filament fracture is induced by high Lorentz forces during SULTAN testing of this prototype toroidal field CICC and that the strand sections with the most damage are located at the petal corners of the high field zone.

(Some figures may appear in colour only in the online journal)

1. Introduction

The ITER superconducting magnet system comprises four types of coils [1]: the toroidal field (TF) coils, the central solenoid (CS) coils, the poloidal field (PF) coils, and the correction coils (CC), in which the superconducting feeder busbars are typically included. The high fields produced by the TF and CS coils require the use of strands using Nb_3Sn superconductor, whereas Nb–Ti-based strands are used in the lower field PF coils and CC [2]. Each cable contains over a thousand strands, each strand transposed along the length of the cable by multiple cabling operations. Short straight sections of the full-size cable-in-conduit conductors (CICC) for these coils have been tested under cyclic loading at currents of typically 68 kA and a background field of 10.78 T at the SULTAN facility at CRPP in Villigen, Switzerland to

explore the ability of these complex conductors to support the high loads and cyclic operation required by ITER.

In 2008, a PF insert coil made of Nb–Ti strands was tested successfully at the Japan Atomic Energy Agency (JAEA) in Naka [3]. This test showed that the PF coil limits were identical to the sum of the strand performances in the cable at the location of the peak magnetic field. Unlike the tough and ductile Nb–Ti, Nb_3Sn is a brittle intermetallic compound with a critical current, I_c, that is highly sensitive to strain [4]. Tests of short (<4 m), straight, full-size ITER TF Nb_3Sn CICC lengths at the SULTAN facility have all shown significant degradation of the current sharing temperature, T_{cs}, in particular during the early stages of electromagnetic (EM) cycling. Multiple effects may contribute to the degradation [5, 6].

From analysis of T_{cs} data on the whole CICC and comparison to the known $I_c(\varepsilon)$ performance of the individual strands in the conductor, it is estimated that the effective axial strain of the CICC after fabrication, cool down and cyclic testing in SULTAN is −0.5 to −0.7% compressive [7]. However, mechanical modeling of the strain state of each strand within the CICC [8, 9] suggests a distribution of strains in each strand on first cool down that varies longitudinally such that each strand suffers both compressive and tensile strains depending on its local position in the fully transposed cable. This large strain variation introduces the possibility that some of the observed irreversible degradation may be contributed by periodic tensile cracking and not just by the compressive strain seen by most of the conductor. The much larger number of cycles needed for the CS conductors does suggest an important need to understand whether compressive or tensile degradations at the individual strand level are dominating the continuous degradation of T_{cs} with cyclic loading. In this paper, we address the question of whether filament cracking is indeed present in a TF CICC after its full test in SULTAN.

In this study we attempt to answer the following questions regarding the T_{cs} degradation of low void-spacing 'option 2' ITER CICC.

(1) Is there significant strand movement within the CICC due to the cyclic electromagnetic loading in SULTAN?

(2) Is there strand damage produced either by cabling or by the electromagnetic loading?

(3) Is there quantifiable filament breakage that can be attributed to magnetic field or warm up–cool down (WUCD) cycling?

These questions were addressed by observing sections of the CICC after testing in the SULTAN facility cut from both the high field zone (HFZ) where the background field is at a 10.78 T plateau, and the gradient-field zone (GFZ) where there is a gradient in field along the length of ∼15 T m^{-1} (figure 1).

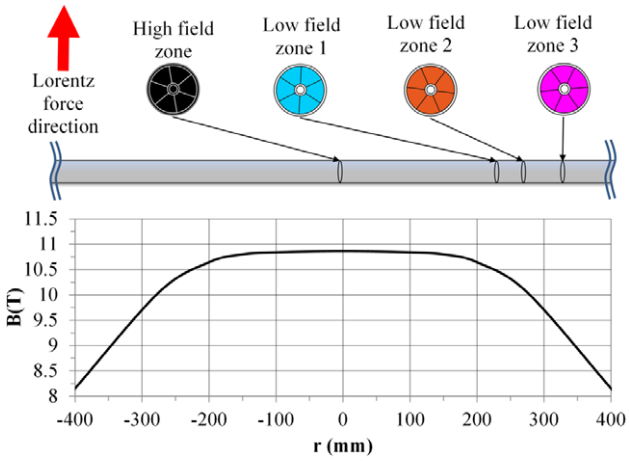

Figure 1. Position of transverse cross-sections analyzed with respect to the background field.

Table 1. Summary of TF conductor specifications.

Cabling layout	(2sc + 1Cu) × 3 × 5 × 5 + core × 6
Core layout	(3 × 4 Cu)
Twist direction	Right hand
Cable twist pitches	80/140/190/300/420 mm
Core twist pitch	80/140 mm
Cable wrap thickness	0.1 mm
Central spiral outer diameter	10 mm
Spiral and wrap material	304L or 316L
Jacket material	316 LN
Jacket thickness	2 mm
Final conductor OD	43.7 mm

2. Experimental details and example results

2.1. TFEU5 cable design

The conductor reported on here is the right leg of the TFEU5 CICC tested at SULTAN in 2010 [10, 11]. This leg is an 'option 2' conductor composed of Nb_3Sn bronze process (BR) strands. 'Option 2' cables are designed with a longer cable twist pitch and lower void space than previous prototype ITER designs in order to improve strand–strand support, and cables using this design have reduced T_{cs} degradation sufficiently to become the standard approach at this time [12]. Each TF CICC is made of 900 Cr-plated Nb_3Sn strands and 522 Cr-plated copper strands. The main parameters of the TF conductors are presented in table 1 [13]. The TFEU5 sustained 1000 full current (68 kA), high field EM cycles (10.78 T background field + self-field = 11.3 T in the high field zone) and one WUCD cycle in SULTAN. The conductor fully met the T_{cs} requirement for an ITER TF conductor during testing, however a T_{cs} degradation of 0.35 K was measured that is in the typical range for this type of conductor [10].

2.2. Cable disassembly and sectioning

After the CICC conductor leg was tested in SULTAN it was shipped in a protective casing to the National High Magnetic

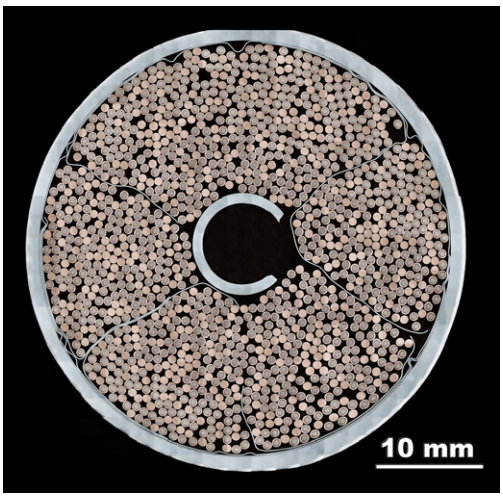

Figure 2. Transverse cross-section of an epoxy impregnated section of the TFEU5 CICC from the high field zone position. The cable has 900 Nb_3Sn and 522 copper strands divided into six sub-cables or petals, each separated from each other by a thin spiral stainless steel wrap with nominal 50% coverage. Part of the outer stainless steel conduit was rounded off to aid uniform polishing of the interior cross-section.

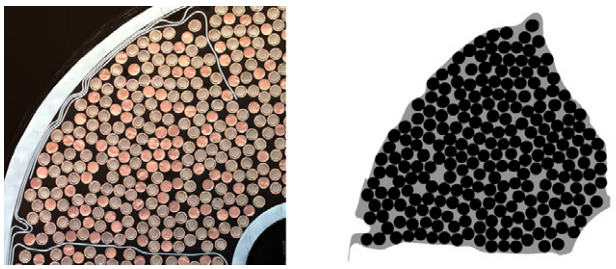

Figure 3. At right is the thresholded image applied to one of the petals in the left hand image. The void space is shown in gray and the strands in black.

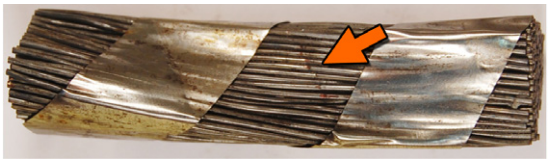

Figure 4. Diagonal surface damage to the outside strands from a (removed) adjacent petal wrap is evident on the center portion of this extracted cable petal from a section cut from the high field zone of TFEU5.

Field Laboratory at the Florida State University, where the whole CICC was first sectioned using electro-discharge machining (EDM) to minimize any damage to the individual strands in the cable as it was cut. The CICC had been scribed at CRPP with the direction of the electromagnetic field loading so that it was possible to track the 'high force' side of the CICC, that is the side of the jacket to which strands are pushed by the Lorentz force acting on the individual strands, and conversely the 'low force' side opposite the 'high force' side of the conductor.

2.3. CICC cross-sectional metallography

After the EDM sectioning, selected 10 cm lengths from the center of the HFZ and the GFZ were vacuum impregnated with epoxy to hold the strands in place. With the epoxy support in place, additional cuts were then made with a diamond saw to obtain multiple transverse cross-sections within the original 10 cm lengths. Figure 2 shows an example of one such transverse cross-section.

Image analysis of the transverse cross-sections revealed that significant redistribution of the void fraction within the CICC did take place during SULTAN testing. We calculated the void percentage within each of the six sub-cables or petals using four different transverse cross-sections

For void fraction calculation, image analysis has been performed earlier [14] using planimetry of enlarged photographic images but here we developed more accurate and quicker methods using freely available software [15] to stitch very large matrices ($\gg$100) of digital images generated by a laser scanning confocal microscope. In this application we do not require the very high resolutions the LSCM is capable of but rather exploit the through-focal image assembly of the microscope to provide us with in-focus imaging across the very large area coverage of the image mosaic.

For all transverse cross-sections, the images are presented with the Lorentz force pointing upwards, making the high force side of the CICC always at the top of the images. One transverse cross-section from the HFZ and three from the GFZ were imaged. A threshold was applied to the images and the void fraction for each petal was calculated using image processing software (Fovea Pro add-in for Adobe Photoshop). Figure 3 shows one such example.

Because of the twisting nature of the cable, it is expected that each petal rotates through 360° with respect to the CICC axis along the cable length. Therefore, in a specific cross-section image the petals are identified by an angular value starting at the twelve noon position (0°) and increasing the angular position in the clockwise direction. This means that the petals with values close to 180° are on the low force side and petals close to 0° or 360° are on the high force side of that particular cross-section.

2.4. Cable disassembly

One (not epoxy impregnated) CICC section obtained from the initial EDM cuts was disassembled to record any damage to the strand surfaces. This section was taken close to the center of the HFZ, approximately from $r = 0$ to -43 mm in figure 1. The outer stainless steel jacket was removed using a diamond saw and the six sub-cable wraps were then unraveled. We observed that strands in direct contact with the wrap often had scratches and indentations on them (see figure 4). Several damaged strands were mounted for metallographic analysis.

In earlier work we used metallographic methods to quantify and describe filament cracking in straight Nb_3Sn strands after they underwent controlled deformation [16–18]. The longitudinal mounting of these straight strands in [16–18] was performed using a pressurized thermoplastic hot

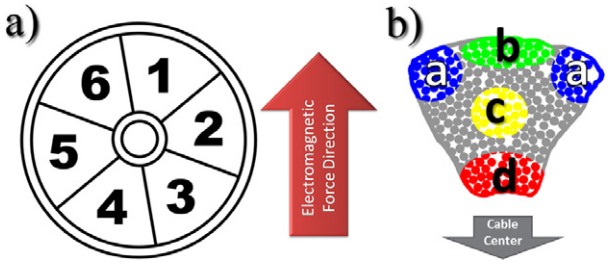

Figure 5. (a) Petal labeling (1–6) with respect to the electromagnetic force direction. 1 and 6 lie on the high-pressure side (b) position within each petal (a–d) with respect to the cable center.

mounting system, but for the twisted and cabled strands studied here, where the strands do not lie flat against the mounting plane, we took the precautionary step of cold mounting the strands in epoxy resin to eliminate the possibility of introducing strain in the pressure-mounting process.

We found that this 'option 2' design has a long enough twist pitch so that strand segments up to ∼15 mm long can be polished in longitudinal cross-section to ∼ half the filament diameter while retaining the filament pack within the polishing plane along most of their lengths before twisting out of view. The sample mounts were carefully polished using techniques similar to those in [17] and finally carbon coated to avoid charging of the epoxy surface during the FESEM imaging.

For analysis of surface damage, several surface-scratched strands (like the ones seen in figure 4) were mounted. FESEM images were then used to determine the magnitude of the damage and when the damage occurred.

2.5. Filament crack observations

The stainless steel jacket was removed from two additional sections of the CICC with the goal of extracting the strands for filament fracture analysis. One section was taken from the HFZ, $r = -43$ to -100 mm (10.78 T peak background field) and another from the GFZ, $r = 340$–390 mm (∼8.3–9 T peak background field). Cable twist has only a small effect on petal position over these small lengths since the full cable twist pitch is 420 mm, making it safe to say that strands extracted from a specific petal on the high or low force side of the CICC are indeed fully typical of that position in the CICC. This allows us, in this case, to label the petals by consistent numbers instead of angles, starting from 1 at twelve noon and increasing petal number in the clockwise direction. Figure 5(a) labels the petals, showing clearly that petals 1 and 6 are high force and petals 3 and 4 low force petals.

The cable modeling of Bajas *et al* [9] predicts that there are certain areas that suffer larger strains under Lorentz force loading, in particular the center and corners of the petals. To allow comparison to this study [9], we analyzed strands from positions a, b, c and d, as seen in figure 5(b).

The strands extracted from HFZ and GFZ are around 50 mm long, short enough to ensure that each strand piece is subject to a similar electromagnetic force vector. However, all strand pieces are part of a continuously transposed and twisted conductor pack that has been quite heavily deformed during cabling and jacketing, making the local geometry of each strand quite variable. In fact, every strand will find itself at some point along the length in a significantly curved position. An important observation of this paper is that filament fracture occurs preferentially in the curved rather than in the straighter sections of strand.

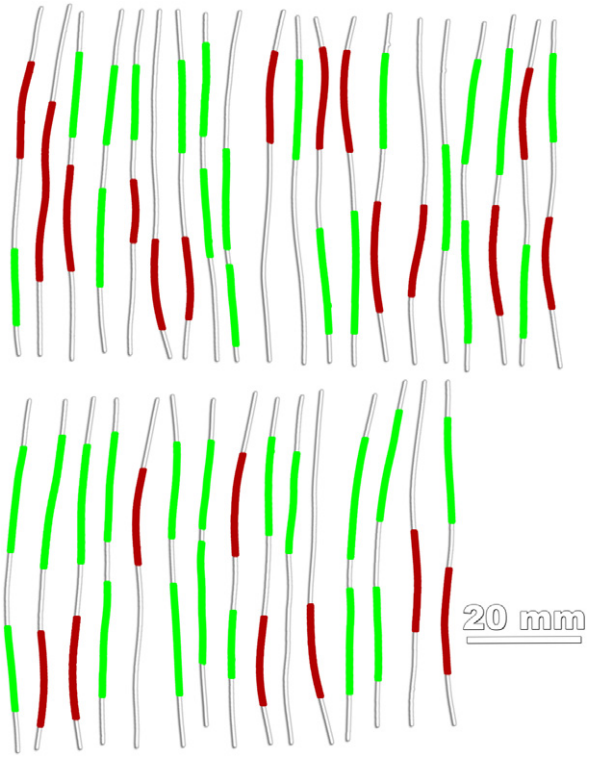

Figure 6. An annotated 2D scan of strands extracted from the HFZ petal 3 position c. Those segments highlighted in red/dark were classified as 'bent' and those highlighted in green/light as 'straight'.

From these 50 mm long sections of strand, we then selected several ∼15 mm long strand segments in order to mount them (as explained in section 2.2) for filament crack analysis. These mounted strand segments can be traced back to their specific petal and position, but each segment has a local shape determined by imposed cable and Lorentz force driven motions. Figure 6 presents a two-dimensional scan of a group of strands extracted from one of the cable sections. It can be seen that the variation of the radius of curvature along the strand length is significant.

This curvature variation is an important characteristic of the strands and necessitated the comparison of not only the effect of the position of the strand within the petal but also the degree of local curvature. For this study we selected and sorted strand segments into two contrasting groups based on their local curvature: 'bent segments' where the radius of curvature was less than 25 mm and 'straight segments', where the radius of curvature was larger than 100 mm.

The scan in figure 6 shows segments classified as 'straight' or 'bent' in green and red, respectively. For statistical purposes this classification was done for a larger

Table 2. Number, type and location of analyzed segments.

Petal number	Number of segments		
	Straight segments from the HFZ	Bent segments from the HFZ	Bent segments from the GFZ
1	6	11	12
2	6	11	12
3	0	11	12
4	0	12	12
5	4	12	12
6	8	5	12
Total	24	62	72

group of strand sections and it was found that around 40% were bent segments and 60% straight segments. The segments selected for analysis were at least 8 mm away from the EDM cut so as to avoid any risk of strain produced by the cutting process. Similarly, the polished cross-section used for crack analysis was >4 mm from the mechanically cut ends of the strands.

Table 2 summarizes the number of strand segments mounted for crack analysis according to their geometry, petal number and zone. We should emphasize that nothing in the broad shape of sections like those presented in figure 6 is inconsistent with the shaping imposed by cabling performed prior to the Nb_3Sn reaction heat treatment and prior to the SULTAN testing. What we can imagine however is that the local environment of the strand permits additional movements under the stresses imposed by cool down and electromagnetic loading.

For the straight segments we quickly realized that filament fracture was rare in all cases, hence the relatively small number of straight segments analyzed. We planned on analyzing 4 'bent' segments for each position a, b, c and d resulting in a total of 12 bent segments from each petal. In some cases we did not reach a total of 12 segments, either because copper strands were mistaken for Nb_3Sn strands or there was too much out-of-plane curvature to reveal a representative length of filament pack. We also isolated fewer superconducting strands from the central location ('c') because this cable layout had a central core of Cu strands.

The filament fracture density varies significantly from zero cracks to as many as 1000 cracks in a single 15 mm strand segment cross-section. The density of these cracks varies locally as well along the length of the strand. These localized crack distributions are remarkably similar to those we have observed in ITER strand samples, provided by the University of Twente, which have undergone controlled localized loading in their TARSIS system [19] designed to simulate strand cross-over loading. To measure the local distribution of crack densities, the crack frequency was measured across a sequence of 100 μm wide bands, each spanning the non-Cu area (the bands are running vertical independent of the curvature of the strand). A single band is shaded in figure 7.

Since the crack density varies along the strand length, we classify the strand segments according to their maximum local crack density, varying from minimal (level 0) to highest (level 5) as shown in table 3, which reports both the peak

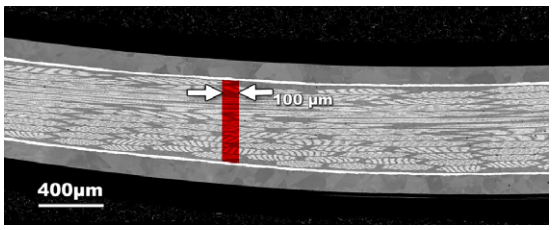

Figure 7. A typical longitudinal cross-section of a strand analyzed with a single analysis band highlighted. The crack density is calculated for each one of the slices along the whole strand length.

Table 3. Crack density classification levels.

Crack density level	Crack density (cracks per mm^2)	Equivalent number of cracks per mm length of filament
Level 1	<150	<0.9
Level 2	150–1000	0.9–5.9
Level 3	1000–2000	5.9–11.8
Level 4	>2000	>11.8
Level 5	>2000 ratcheted	>11.8 ratcheted

crack density range and its equivalent number of cracks per mm of Nb_3Sn filament obtained by multiplying the crack density per unit area by the length of filament exposed in the given area. For the strands analyzed here there is about 170 mm of filament exposed per mm^2. Figure 8 shows images corresponding to these different crack density levels.

Crack density levels 1–3 were earlier observed in TARSIS-tested strands, level 3 being equivalent to the crack concentration found at the highest strain developed in TARSIS samples loaded at 10 kN m^{-1} which produce an I_c degradation of more than 30% [19]. Crack density levels 4 and 5 exceed any of our previous TARSIS observations, level 5 cracks are both denser and much wider than those found at lower crack density levels, with clear evidence of a ratcheted crack opening under electromagnetic cycling.

3. Detailed results

Below we organize the results of this work according to the three driving questions of the work, paying attention to the location of the samples with respect to the position along the cable, as summarized in figure 1.

3.1. Strand shift under load and the resulting void fraction redistribution

The void fractions measured here are the areas within individual petals that are not occupied by strands expressed as a percentage of the petal areas. Figure 9 shows the void fraction deviations (normalized deviations from the average values for all cross-sections and petals) for all cross-sections plotted against the angular position of the petal with respect to the Lorentz force direction. The normalized void fraction is negative when the petal has undergone a compression (i.e. there is less void fraction) and it is positive when the petal

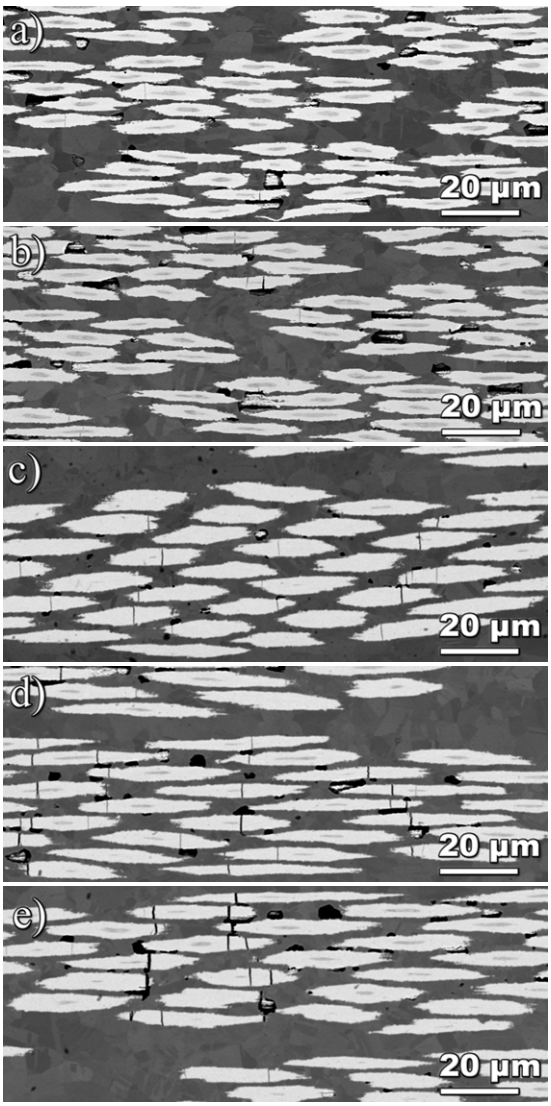

Figure 8. Crack density levels (a) level 1 (b) level 2 (c) level 3 (d) level 4 (e) level 5.

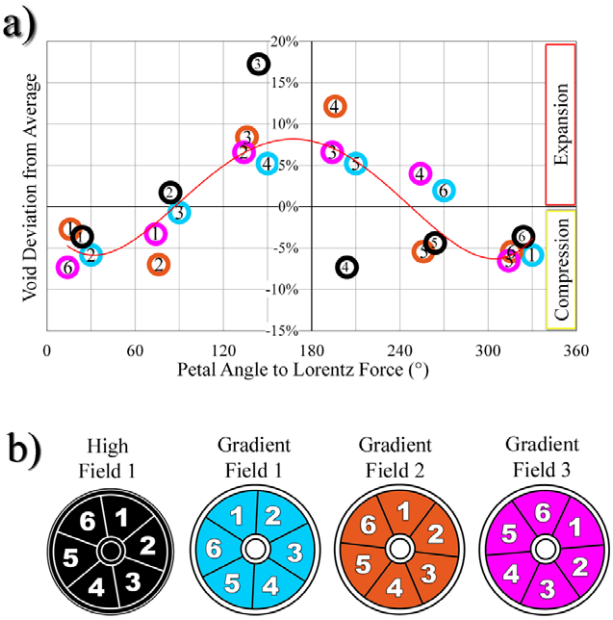

Figure 9. (a) Petal void redistribution after EM cycling. 0° represents the high force side of the cable and 180° represents the low force side of the cable (b) color key.

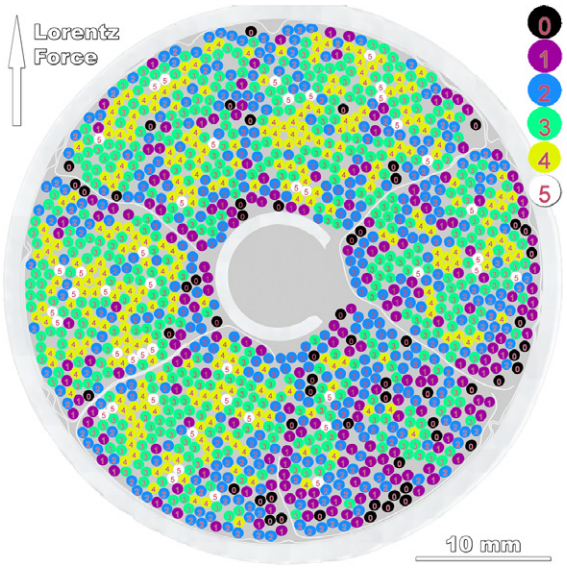

Figure 10. Transverse high field zone cross-section with the strands shaded according to the adjacent strand count (i.e. number of nearest-neighbor strands), which ranges from 0 to 5 (most densely packed).

has undergone an expansion. Although there is some scatter, it is clear that there is a quasi-sinusoidal distribution of void fraction, which is about 10% denser on the high force side (0° or 360°) and correspondingly less dense on the low force side (180°). Most of the scatter comes from petal 4 of the high field cross-section (black). This is proportional to the large expansion suffered by petal 3 (almost 17%) suggesting that the strand movement within the petal is not independent of adjacent petals.

In figure 10 we illustrate how the movement of the strands has changed the local strand–strand support by counting the number of nearest-neighbor strands. This is possible by first artificially separating touching strands by one pixel (most filaments touch each other making an otherwise agglomerated object that is not useful for measuring individual strand movement) and then counting the number of filaments that are connected by a single pixel-wide four-connected (i.e. continuous) line. Thus the adjacent filament count is the number of filaments within 2.5 μm (1 pixel at this resolution) of a particular filament. The cross-section in figure 10 corresponds to the high field cross-section in figure 9. The predominance of dark shaded filaments in the lower right hand petal (petal 3), shows that the strands have moved away from each other increasing the void fraction significantly and implying a reduction in strand-to-strand mechanical support. Conversely the adjacent low force petal (petal 4) remains densely packed.

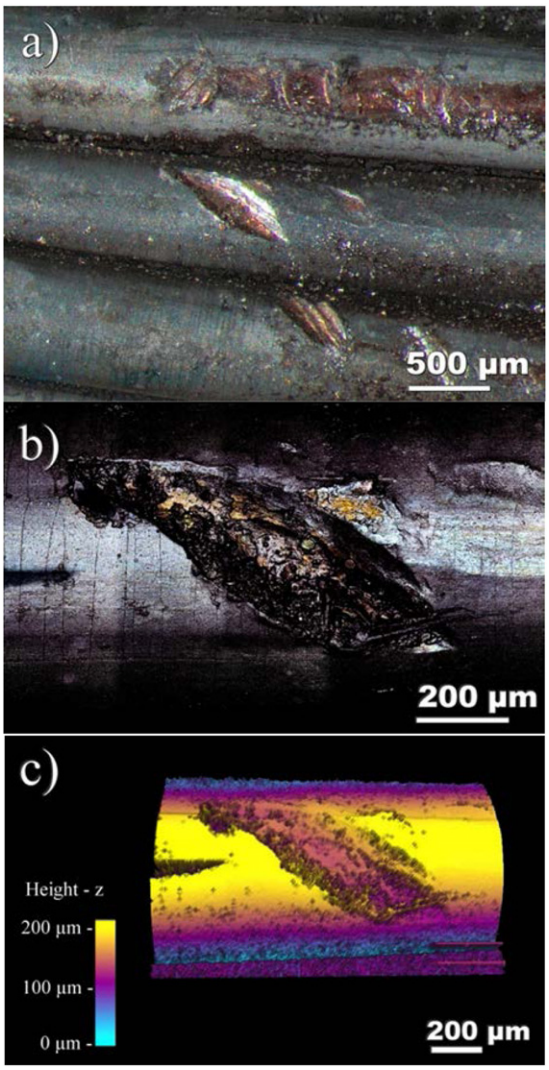

Figure 11. (a) The edges of the sub-cable wrap often left behind indents like this one. (b) a LSCM image of the indented area. (c) A 3D image of the indented area.

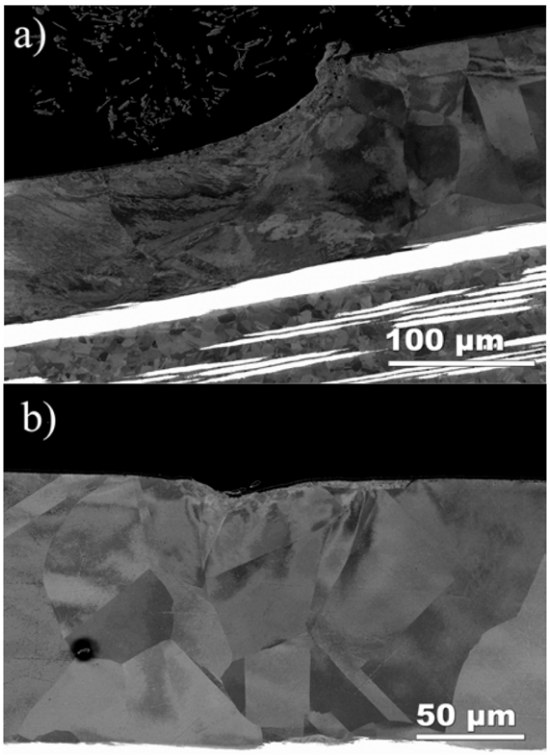

Figure 12. TFEU5 scratched strands. There is clear evidence of cold work under the scratch indicating that it occurred AFTER reaction under the cooling, warming or electromagnetic loading in SULTAN.

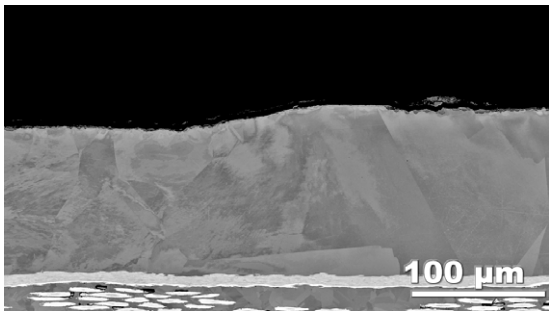

Figure 13. Pinched surface of a crossing TARSIS strand indented at 10 kN m^{-1} (strand sample courtesy of A Nijhuis of the University of Twente).

3.2. Surface Strand Damage

Some deeply indented strands of the type shown in figure 4 were imaged using the laser scanning confocal microscope (LSCM) to measure the scratch depth. Figure 11 shows one of the worst cases, an indentation 63 μm deep, almost halfway through the copper annulus.

We have also taken several electron backscatter FESEM images to reveal the copper grain structure around the damaged area of the strands. Figure 12 shows two micrographs of TFEU5 strands with surface damage, while figure 13 shows the pinched surface of a crossing TARSIS strand [19]. The Cu grain structures for all these images show heavily cold worked copper grains around the damaged area, an indication of damage that has occurred after cabling, jacketing, and SULTAN sample preparation because the final Nb_3Sn reaction heat treatment is much more than is required to fully anneal the Cu stabilizer; thus the damage occurred either under cool down or under cyclic loading. It is clear that the damage observed in the TFEU5 strand is much greater than any produced in the TARSIS testing, perhaps reflecting the fact that TARSIS damage is induced by strand crossing and the TFEU5 damage by indentation of the stainless steel petal wrap into the soft (annealed) Cu annulus but also indicative of very high local forces in the conductor elements.

3.3. Filament fracture observations

Table 4 summarizes the crack concentration measurements. The contrast in the crack concentrations between 'straight' and 'bent' segments is quite striking, with 96% of straight segments from the HFZ being crack free while only 52%

Table 4. Number of segments with specific crack density, classified by zone and geometry.

	Number of segments		
Crack concentration level	Straight segments from the HFZ	Bent segments from the HFZ	Bent segments from the GFZ
0	23	32	42
1	0	15	19
2	1	12	10
3	0	0	1
4	0	1	0
5	0	2	0
Damaged	4%	48%	42%
Crack free	96%	52%	58%
Total	24	62	72

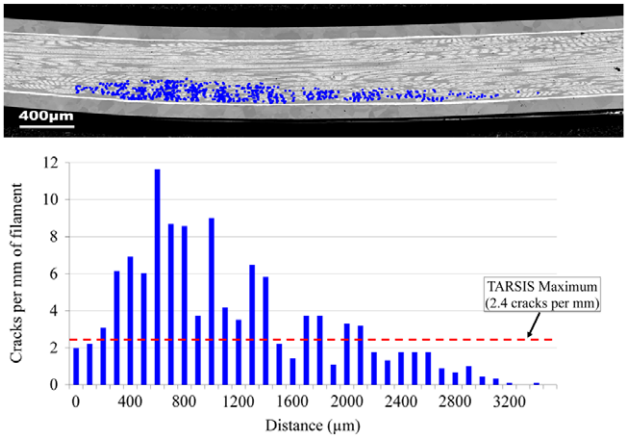

Figure 14. Level 5 cracks found in a HFZ strand along the strand length. The histogram displays the crack concentration (per 100 μm width band: figure 7) variation along the length of the analysis region. For reference, the dotted line represents the maximum crack concentration that we have observed in TARSIS-tested strands.

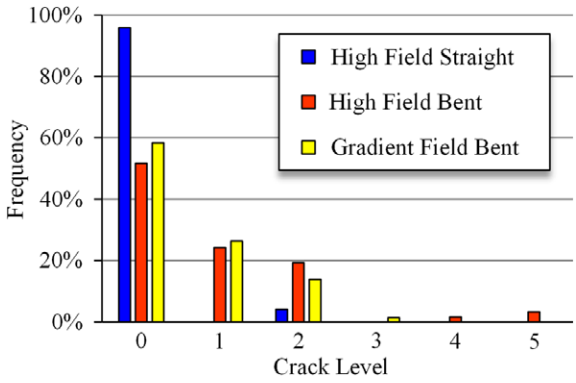

Figure 15. Percentage of segments containing the specified crack density level within their respective group. Note that crack level zero means that cracks were not seen, meaning that most strands were not damaged.

of the bent segments in the HFZ were crack free. Very high levels of filament damage were observed in some bent segments. Figure 14 shows a histogram of the very high, level 5 crack density observed in a curved segment extracted from petal 3 in the high field zone. It is clear that there is a local maximum crack density and a quasi-Gaussian decay away from the maximum that is localized to a length of about 3 mm. These cracks concentrate on the outer side of the bend, as was the case for every studied strand segment, regardless of crack density. The dotted line on the graph represents the significantly lower (level 3) maximum crack concentration that we analyzed for controlled TARSIS-tested strands from Twente—corresponding to 10 kN m^{-1} loading (the heaviest loading the TARSIS samples supplied by Twente). The implication of finding localized cracks on the outer bend surface in figure 14 is that there has been an additional bend strain under SULTAN testing that has produced sufficient tensile strain on the outside of the bend that filament fracture becomes possible.

The percentages of damaged segments are represented graphically in figure 15 by crack concentration level. Notice that in the HFZ, the population of damaged segments contains crack density levels 1–5, while in the GFZ it varies only from 1 to 3, suggesting that the drop in overall Lorentz force (the lowest GFZ background field is 23% less than HFZ background field) is sufficient to eliminate the worst levels of cyclic damage but does not eliminate filament cracking. These very high levels of filament fracture on the HFZ only could also be attributed to the softening of the cable's HFZ segment suspected by Mitchell *et al* [6].

Figure 16 plots the distribution of damaged strands by petals. In this case there is the appearance of a trend from petal to petal in sequence from petal 1 to petal 6 but as both petals 1 and 6 are 'high force' there does not appear to be a direct relationship between crack density and the direction of the Lorentz force. Perhaps this is not surprising because as the strands become more densely packed on the high force side during testing, their ability to cyclically bend becomes more restricted, and conversely for the low force side where the strands become relatively less restricted and thus the amplitude of bending is likely to change in a complex manner over the duration of the test. Our analysis of crack locations indicates that localized pivot points with small radius of curvature have the greatest influence on crack density, rather than a simple global shifting of the strands inside a petal. The degradation produced at these local pivot points can be enhanced by stronger Lorentz forces acting on the HFZ, hence the high levels of filament fracture seen in the HFZ.

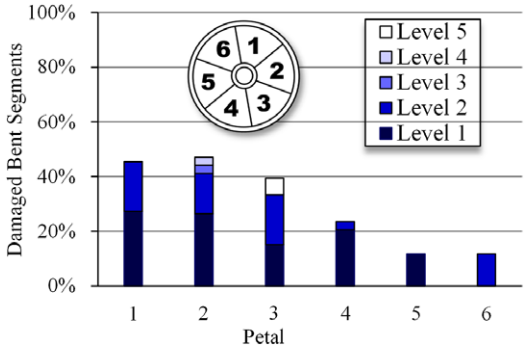

Figure 16. Percentage of all damaged bent segments from both HFZ and GFZ sorted by petal.

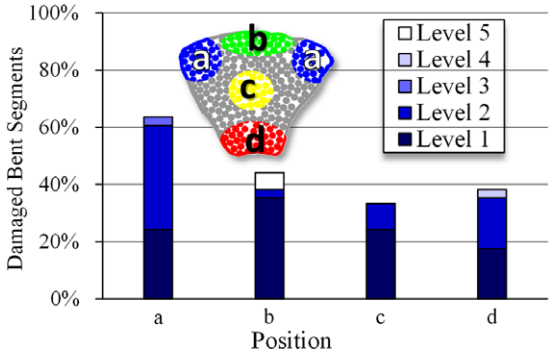

Figure 17. Percentage of damaged bent segments from both HFZ and GFZ and from all petals sorted by position. The population of damaged strands is higher for the petal corners.

In figure 17 the crack concentrations for all segments are broken down by the four locations of interest within the sub-elements. The location of the highest crack concentration is position 'a' at the outer corners of the sub-element.

4. Discussion

We started the study with three questions in mind.

(1) Is there significant strand shifting within the CICC due to the cyclic electromagnetic loading that occurs in SULTAN?
(2) Is there strand damage produced either by cabling or by the electromagnetic loading?
(3) Is there quantifiable filament breakage that can be attributable to magnetic field or WUCD cycling?

The first question posed by our inquiry was whether there was significant strand shifting within the CICC due to the cyclic electromagnetic loading in SULTAN. It is remarkably clear for even this dense (30% void) long twist pitch 'option 2' cable design that the strands within the CICC move significantly in the direction of the Lorentz force, reducing the void fraction on the high stress side of the conduit as strands are pushed by their neighbors. The highest increase in void space was located in the HFZ (petal 3) which saw a 16% void fraction increase in an HFZ sample on the low force side. There is thus considerable 'bedding down' of the conductor under the large Lorentz forces, presumably leading to additional local strand bending strains, particularly at strand crossing points.

In an attempt to confirm this additional local bending we explored the copper grain structure of strands like that in figure 14, looking for evidence of work hardened areas. Figure 18 shows a larger view of this strand and three different inserts of different copper areas. The grain structure of the copper throughout most of the image resembles that of

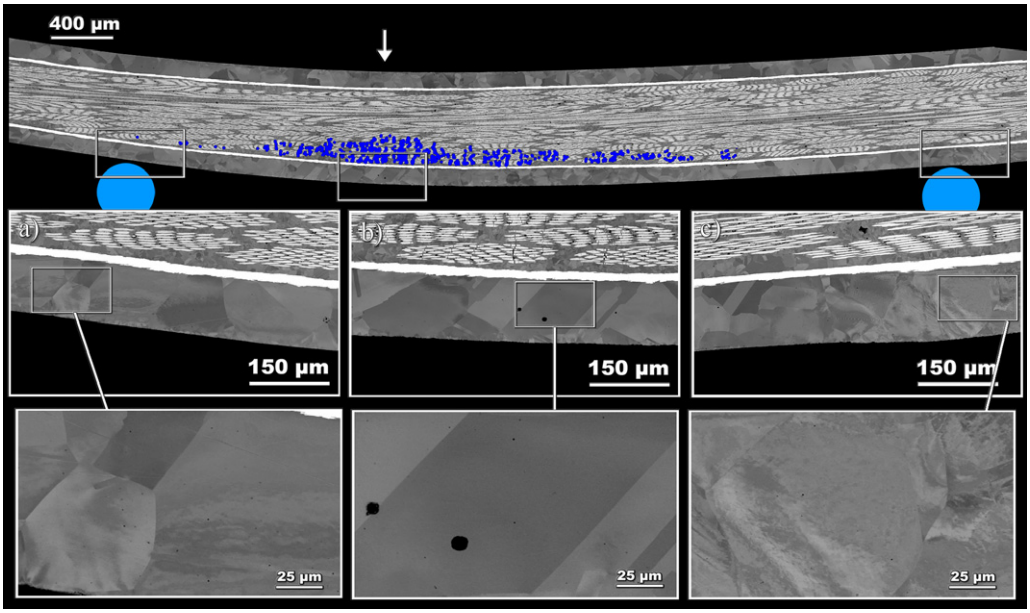

Figure 18. Level 5 cracks found in a HFZ strand along the strand length showing inserts of cold worked copper suggesting pivoting points. The red dots indicate where the neighboring strand was introducing two pivot points that induce this bending moment.

inset (b) with very well defined grain boundaries and strain free grains. Areas (a) and (c) are the exception. Here, the grain boundaries are less defined and show dislocations and irregularities similar to those seen in figure 13 suggesting cold worked copper. This is clear evidence of strand-to-strand contact points acting as pivot points that allow for additional bending. These contact points are represented by the blue dots on the image. In fact, inset (c) shows deformation caused by the neighboring strand.

Similar filament fractures seen in [16] are produced by a bend with a radius of curvature of ∼40 mm (starting from a straight strand). The similarities in filament fracture concentration of these 40 mm radius of curvature strands to those seen in figures 14 and 18 suggest that there should be additional bending during the electromagnetic cycling of the cabled strands, and this additional bending is comparable to the change in curvature seen in [16].

Concerning the second question as to when observable damage to the strand surface of the sort depicted in figures 11–13 occurs, there seems to be a clear answer. Figure 12 shows unambiguous evidence of elongated Cu grains under the indent. Since Cu anneals only on being heated above about 450–500 °C and the reaction heat treatment of the wire includes steps of 575 and 650 °C each for 100 h, it is quite clear that cold work done before reaction would have been removed during reaction. Thus we can conclude that the indentation occurred after cabling and after reaction and that either thermal strain during cooling to low temperatures or the Lorentz force loading itself must be implicated in this damage. However, it also appears that this damage is restricted to the Cu annulus around the diffusion barrier and that it did not cause any filament damage. Thus the net impact of this surface deformation due to sub-cable wrap, though not very pretty, is without functional impact on the conductor. This conclusion is also consistent with similar postmortems on flow under crossing strands tests in TARSIS, as shown in figure 12.

As to question 3, it is clear that there is abundant evidence for local filament damage, though even in the most damaged strands, the damage never occurs across the whole cross-section and remains clearly localized axially too. These are both signs that the damage occurs due to local strain intensification. We find that cracking is most strongly correlated to local strand curvature, curved strand lengths being ten times as likely to contain fractured filaments as straight strands. The highest crack densities found in the TFEU5 CICC were four times higher than in the worst case of bending strain tested in TARSIS under 10 kN m^{-1} loads. But as alarming as our crack observations might seem, such a high crack level was only seen in 3% of the curved strands from the HFZ samples. Thus, it is important to highlight that cracking is rare and appears to be confined to special regions where local tensile strains are large enough to produce filament fracture. The implication in particular of figure 14 is that the driving force for filament fracture is bend strain, since the filament cracks are clearly confined to one side of the conductor and appear on the outer radius, consistent with an additional tensile strain produced by bending. Local bending is of course to be expected as ubiquitous under the Lorentz force loading and to be exacerbated by the gross movement addressed by question 1 of this paper.

An interesting question is whether postmortem deconstructions such as this can validate the interesting predictions of cable modeling efforts such as those of Bajas *et al* [8, 9].

The important question is of course what significance these deconstructions of a fully tested ITER TF CICC have more generally for ITER conductors, given that lowered T_{cs} after cyclic loading can be the result of degraded superconducting properties produced by both compressive and an increasing tensile strain on the conductor. The implications of these effects for the central solenoid conductors which must withstand 60 000 rather than the 2000 cycles of the TF coils may be significant. If the effect of cyclic Lorentz force loading is primarily to work harden the bronze surrounding each Nb_3Sn filament, this is likely to saturate, thus leading to a T_{cs} that should saturate with increasing cycle count. A tensile strain component that can cause filament cracking is much more likely to prevent saturation of its degrading effect on I_c and T_{cs}. Figure 14 especially shows how small additional bend strains can produce cracking on the tensile side of a curved strand, while figures 9 and 10 show that there is significant movement of strands under the cyclic loading that can produce such critical bending. There is clearly opportunity for damage and a more targeted study of this effect is clearly warranted.

5. Conclusion

In this paper we have presented a detailed and quantitative metallographic study of a fully SULTAN-tested, full-size ITER TF CICC. The analysis shows that there is significant movement of the strands within the CICC. It also shows that significant strand surface damage occurs by indentation of the stainless steel wrap after cabling and during testing. Local filament cracking was seen in curved strand segments but little in straighter strand segments. Taken in their totality, the conclusion is that Lorentz force cycling induces movement of the strands within the CICC and sets up conditions such that especially strongly curved strands can develop tensile strains on their outer surfaces that can cause filament fracture at quite high, localized densities.

Acknowledgments

The work was funded by a contract initiated by Neil Mitchell from the ITER Organization but benefited from additional funding by the State of Florida and US DOE Office of Fusion Energy Science (Grant DE-FG02-06ER54881). The SULTAN-tested cable was provided by courtesy of Pierluigi Bruzzone (Plasma Physics Research Center) with agreement from Fusion for Energy. The views and opinions expressed herein do not necessarily reflect those of the ITER organization.

References

[1] Mitchell N *et al* 2007 The ITER magnet system *IEEE Trans. Appl. Supercond.* **18** 435–40

[2] Devred A *et al* 2012 Status of ITER conductor development and production *IEEE Trans. Appl. Supercond.* at press
[3] Bessette D *et al* 2009 Test results from the PF conductor insert coil and implications for the ITER PF system *IEEE Trans. Appl. Supercond.* **19** 1525–31
[4] Ekin J W 1980 Strain scaling law for flux pinning in practical superconductors. Part 1: basic relationship and application to Nb_3Sn conductors *Cryogenics* **20** 611
[5] Schultz J H *et al* 2005 Transverse stress effects in ITER conductors *IEEE Trans. Appl. Supercond.* **15** 1371–4
[6] Devred A *et al* 2003 Summary, assessment and implications of the ITER model coil test results *Fusion Eng. Des.* **66–68** 971–93
Devred A *et al* 2003 *Cryogenics* **43** 255–70
[7] van Lanen E P A and Nijhuis A 2011 Numerical analysis of the DC performance of ITER TF samples with different cabling pattern based on resistance measurements on terminations *Supercond. Sci. Technol.* **24** 085010
[8] Bajas H, Durville D, Ciazynski D and Devred A 2010 Numerical simulation of the mechanical behavior of ITER cable-in-conduit conductors *IEEE Trans. Appl. Supercond.* **20** 1467–70
[9] Bajas H 2011 Numerical simulation of the mechanical behavior of the ITER cable-in-conduit conductors *PhD Dissertation* École Centrale Paris, pp 148–50
[10] Bruzzone P *et al* 2010 Status report of the SULTAN test facility *IEEE Trans. Appl. Supercond.* **20** 455–7
[11] Breschi M *et al* 2012 Results of the TF conductor performance qualification samples for the ITER poject *Supercond. Sci. Technol.* submitted
[12] Nijhuis A and Ilyin Y 2006 Transverse load optimization in Nb_3Sn CICC design; influence of cabling, void fraction and strand stiffness *Supercond. Sci. Technol.* **19** 945–62
[13] Sborchia C *et al* 2011 Overview of ITER magnet system and european contribution *IEEE/NPSS 24th Symp. Fusion Engineering* pp 1–8
[14] Decool P, Cloez H and Cantone V 2007 Investigation on thermal strain in sultan samples *EURATOM-CEA AIM/NT-2007.014*
[15] MICE http://research.microsoft.com/en-us/um/redmond/groups/ivm/ice/
[16] Jewell M C 2008 *The Effect of Strand Architecture on the Fracture Propensity of Nb_3Sn Wires* (Madison, WI: UMI Dissertation Publishing)
[17] Sheth M K 2011 Fatigue behavior of Nb_3Sn composite strands used for ITER magnets *MS Thesis* The Florida State University
[18] Jewell M, Lee P and Larbalestier D 2003 The influence of Nb_3Sn strand geometry on filament breakage under bend strain as revealed by metallography *Supercond. Sci. Technol.* **16** 1005–11
[19] Nijhuis A, Ilyin Y, Abbas W, Wessel W A J, Krooshoop H J G, Feng L and Miyoshi Y 2006 Summary of ITER TF Nb_3Sn strand testing under axial strain, spatial periodic bending and contact stress *Supercond. Sci. Technol.* **19** 1089–96